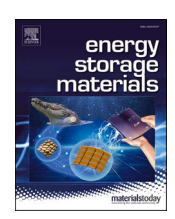
ELSEVIER

Contents lists available at ScienceDirect

Energy Storage Materials

journal homepage: www.elsevier.com/locate/ensm





In-situ constructed protective bilayer enabling stable cycling of LiCoO₂ cathode at high-voltage

Hao Zhang ^a, Yuxiang Huang ^a, Yue Wang ^b, Lu Wang ^a, Zhibo Song ^a, Haoliang Wang ^a, Caixia Xu ^b, Xingtao Tian ^b, Siyu Wang ^b, Jianjun Fang ^a, Wenguang Zhao ^a, Hongbin Cao ^a, Xiangming Yao ^a, Jie Yang ^c, Rui Tan ^d, Luyi Yang ^{a,*}, Feng Pan ^{a,*}, Yan Zhao ^{a,*}

- ^a Peking University Shenzhen Graduate School, Shenzhen 518055, China
- ^b PLA Army Chemical Defense College, Beijing 102205, China
- ^c National University of Singapore, 117546, Singapore
- d University of Warwick, Coventry CV4 7AL, UK

ARTICLE INFO

Keywords: Tris(perfluorophenyl)borane Lithium bisoxalatodifluorophosphate Lithium tetrafluoro(oxalato)phosphate Layered oxide cathode LiF-rich Cathode-electrolyte interphase

ABSTRACT

The practical application of high-voltage lithium cobalt oxide (LCO) has been hampered by the severe degradation of its structural integrity. In this work, a protective bilayer was fabricated on LCO surfaces by means of large-scale and facile electrolyte engineering. The protective bilayer consisting of a LiF-rich cathode-electrolyte interphase (CEI) as the outermost layer and a layer of disordered spinel structure as the inner layer was uniformly fabricated *in-situ*. The high-resistance CEI layer inhibited the fast transfer of Li ions from LCO to bulk electrolyte during the first few cycles, resulting in the significantly increased local overpotential on the LCO surface. As a consequence, the LCO surface underwent a phase transformation from the layered phase to the spinel phase first, forming the spinel phase inner layer due to the voltage rising beyond 4.55 V (vs. Li/Li⁺). The CEI and spinel layers effectively blocked the dissolution of transition-metal (TM) ions into the electrolyte during cycling and inhibited the formation of the structurally defective rock-salt phase that would hasten cycling-induced structural degradation. The formation of the protective bilayer effectively prevented the phase transition from the bulk layered LCO structure into spinel and then rock salt, thereby reducing decay of its cycling capacity. Remarkably, the graphite||LCO pouch cell with optimized electrolyte retained 78.9% of its capacity even after 1000 cycles under the operation voltage window of 3.0–4.55 V (vs. Li/Li⁺). This study provides guidance for the development of effective surface treatment strategies for stable layered cathodes with high capacity and cyclability.

1. Introduction

Lithium-ion batteries (LIBs) are widely used for energy storage due to their long lifespan and high energy density [1–3]. As one of the most popular cathode materials, LiCoO2 (LCO) has garnered increased attention from academia and industry due to its high theoretical capacity (274 mAh g $^{-1}$), high volumetric energy density, and good Li $^+$ /electrons conductivity [4,5]. Despite its increasing price [6,7], markets of LCO cathode materials continue to flourish, particularly in 3C electronic devices. However, the low charging cut-off voltage of 4.45 V (vs. Li/Li $^+$) currently used for LCO significantly restricts its practical capacity to approximately 170 mAh g $^{-1}$ [4,8]. Typically, when charged to voltages higher than 4.5 V (vs. Li/Li $^+$), the deleterious phase transition occurs from the O3 hexagonal phase to the H1-3 hybridized phase

[5]. This detrimental transition increases the internal strain, leading to cracks and pulverization of $LiCoO_2$ particles, ultimately resulting in irreversible phase transitions and serious performance degradation [9–12]. Besides the failure of bulk structures, surface instability is another critical factor that plays a vital role in electrode material stability [9]. The high-valence Co content on LCO surfaces can trigger the oxidative decomposition of the electrolyte, while oxygen loss and cobalt dissolution occurs from the surfaces to its cores, exacerbating irreversible phase transition and serious performance degradation of LCO at high voltage [13–16].

Many strategies have been proposed to enhance the cycle stability of LCO under high voltage conditions [4,10,17–24]. Element doping and surface coating are the most effective techniques identified to date [17, 23–28]. However, element doping reduces the specific capacity of LCO

E-mail addresses: yangly@pkusz.edu.cn (L. Yang), panfeng@pkusz.edu.cn (F. Pan), zhaoyan@pku.edu.cn (Y. Zhao).

^{*} Corresponding authors.

and increases the complexity of industrial production due to the demanding process requirements [17]. Additionally, although surfacing coating can improve the electrochemical performance of LCO in some cases, most coating layers lack of self-healing capability, thus diminishing the coating's effectiveness over repeated cycles. Therefore, there is a pressing need to devise a straightforward approach for enhancing the cycling stability of high-voltage LCO. Optimizing the electrolyte composition is a viable approach to address the challenges by establishing a dense and effective cathode-electrolyte interface (CEI) film on the surface of LCO [14,29-36]. A robust CEI enables fast Li-ion transmission, isolates LCO from electrolytes, restricts irreversible phase transformation, and Co dissolution [31]. Electrolyte solvents optimization is one of the most wildly utilized strategies. Recently, Wang et al. [31] designed an all-fluorinated electrolyte containing 1.0 M LiPF₆ in fluoroethylene carbonate / methyl (2,2,2-trifluoroethyl) carbonate / 1, 1,2,2-tetrafluoroethyl-2,2,3,3-tetrafluoropropylether (FEC/FEMC/TTE) with 2 wt% tris(trimethylsilyl)borate (TMSB) as an additive. The electrolyte demonstrated high oxidation resistance, leading to a robust CEI and stable cycling of single crystal LCO at 4.6 V (vs. Li/Li⁺) with 75% capacity retention after 300 cycles at a current density of 0.5C. However, the utilization of all-fluorinated solvents in solvent regulation may increase the cost and contradict industrial production. Hence, introducing sacrificing additives into commercial electrolytes is a cost-efficient and effective strategy for enhancing interface stability. For instance, Yang et al. [34] used Potassium Selenocyanate (KSeCN) as an electrolyte additive in a high-voltage LCO cathode system and achieved roughly 60% capacity retention after 940 cycles at 4.6 V (vs. Li/Li⁺), owing to the formation of a compact and robust CEI.

Phosphorus-based lithium bisoxalatodifluorophosphate (LiDFBP) is a promising electrolyte additive that can form stable CEI on cathode materials [37–44]. However, LiDFBP production process is always accompanied by large quantities of by-products, including lithium tetrafluoro(oxalato)phosphate (LiOTFP) that has low solubility in a carbonate-based electrolyte, almost less than 1 wt%. Purifying LiDFBP not only increases production and utilization costs but also wastes the valuable additive LiOTFP. In this work, we directly introduced LiDFBP mixtures containing 40 wt% LiOTFP into the baseline electrolyte (1.0 M LiPF6/EC-EMC-DMC=1/1/1 v%) with tris(perfluorophenyl)borane (TPFPB) as the co-solvent. The as-prepared electrolyte was observed to form a dense, robust, and thick cathode-electrolyte interphase (CEI) layer comprising massive B-containing, P-containing and LiF inorganic composition on the lithium cobalt oxide (LCO) cathode. The CEI layer

stabilizes the surface and bulk structure of the LCO cathode, inhibiting Co dissolution and irreversible phase transition of the LCO surfaces. Further characterization showed that after several activation cycles, a thin Co_3O_4 spinel phase surrounded by the CEI occurred at the LCO surface, further protecting the LCO bulk from irreversible phase transition (Fig. 1). As a result, the Li||LCO half-cell using this electrolyte exhibited 80.1% capacity retention after 400 cycles at a current density of 200 mA g $^{-1}$ between 2.7 and 4.6 V (vs. Li/Li $^+$). The optimized electrolyte used in the fabricating graphite||LCO pouch cell displayed excellent long cycling stability, retaining approximately 78.9% capacity after 1000 cycles at 1C. This research provides a practical approach for electrolyte optimization in high-voltage LIBs.

2. Experimental section

2.1. Materials

Commercial LCO material was purchased from WeiMing Co., Ltd., China. The artificial graphite material was purchased from Shenzhen BTR Tech Co., Ltd., China. The baseline electrolyte (BE) comprising 1.0 M LiPF₆ in EC/EMC/DMC=1/1/1 was purchased from DodoChem. The TPFPB co-solvents was purchased from Ark Tech Co., Ltd. and LiDFBP additive was purchased from Changsha T-rock Biochem Co., LTD. The designed electrolyte (DE) was obtained by adding specific amounts of TPFPB and LiDFBP mixture into BE in the Ar gas-filled glovebox of MIKROUNA. The cathode for coin cells comprised 90 wt% active LCO, 5 wt% Super P and 5 wt% polyvinylidene fluoride (PVDF) while the anode comprised 70 wt% graphite, 20 wt% Super P, 4 wt% sodium carboxymethyl cellulose (CMC), and 6 wt% styrene butadiene rubber (SBR). The anode for pouch cells was composed of 94.5 wt% graphite, 2.5 wt% Super P, 1.5 wt% CMC and 1.5 wt% SBR while the cathode was composed of 97 wt% cathode material LCO, 1.5 wt% Super P, and 1.5 wt % PVDF. The mass loadings of graphite anodes and LCO cathodes for coin cells were about 2.0 and 6.8 mg cm⁻², respectively. The mass loadings of the graphite anode and the LCO cathode for pouch cells were 10.2 and 16.2 mg cm⁻², respectively. Each pouch cell was filled with 6 g of the electrolyte.

2.2. Electrochemical measurements

All the coin cells mentioned in the paper were assembled by CR2032 coin cells in the argon-filled glovebox with Celgard 2400 (16 mm in

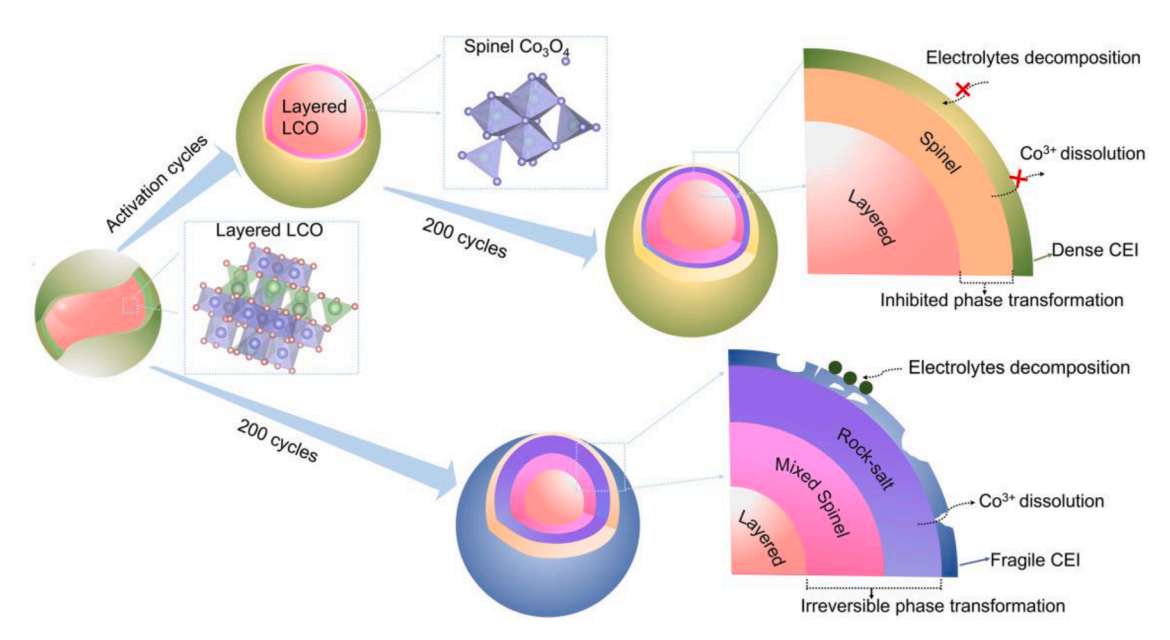


Fig. 1. The scheme of proposed dual-protective layer for LCO cathode.

diameter) as separator. Then the assembled coin cells were tested on a NEWARE battery test system. The pouch cells were performed using the constant current (CC) charging and discharging profile and 10 s rest was implemented after every cycling. Liner sweep voltammetry (LSV), cyclic voltammetry (CV) and electrochemical impedance spectroscopy (EIS) were tested on the Solartron Analytical 1470E electrochemical workstation. LSV and CV curves were tested with a scan rate of 0.5 and 0.2 mV s $^{-1}$ respectively. The frequency range of EIS from 1000 kHz to 0.1 Hz with the AC signal amplitude of 10 mV.

2.3. Characteristics

Raman data and FTIR spectra were collected using a Laser Confocal Raman Spectrometer (Renishaw InVia) and a Nicolet Avatar 360 spectrophotometer (KBr tablet), respectively. Nuclei magnetic resonance (NMR) spectra (1H NMR and 13C NMR) were recorded using Bruker DPX 400 MHz spectrometers. The crystal structure of the samples was analyzed using a Bruker D8 Advance diffractometer (with Cu Ka radiation, at $\lambda = 0.154$ nm) for XRD analysis. Elemental analysis was conducted using ICP-OES (HORIBA JY2000-2). A scanning electron microscope (SEM, Zeiss SUPRA-55) with an X-Max EDS detector was used for the investigation of the morphology and elemental distribution of the samples. The in-suit Ultraviolet and Visible (UV) spectrum was performed on the UV-2450 spectrophotometer. TEM samples were prepared using the FIB, and HRTEM was performed using a JEM-100F microscope. X-ray photoelectron spectrometry (XPS) on a Thermo Scientific Escalab 250Xi spectrometer was used to investigate the chemical states of the selected elements.

2.4. Computational details

To investigate the dissolution characteristic and the impact of the added TPFPB and LiDFBP mixture on the CEI film-forming ability of electrolyte, quantum chemistry calculations were implemented to predict binding energies and the frontier molecular orbital energy of solvents and additives using the Gaussian 09 program package. The

calculations were all performed at B3LYP/6–311G (d) level. The binding energies were defined as the energy differences between the different molecules, namely the binding energy $=E_{ab}-E_{a}$ - $E_{b}.\;$

3. Result and discussion

3.1. Dissolution characteristics of LiDFBP mixture

To generate LiDFBP according to previous reported [45,46], LiOTFP is often generated alongside, which has low solubility in carbonate-based solvent. Further purification procedures lead to increased production expenses and unnecessary waste of promising Li salt additive LiOTFP. A LiDFBP mixture containing 40 wt% LiOTFP can be used directly only after increasing the solubility of LiOTFP in carbonate-based electrolytes. This issue can be addressed by adding electron-withdrawing TPFPB as co-solvent additives [47–50]. As can be observed from Fig. S1, upon the addition of 0.5 wt%, 1.5 wt% and 2 wt% of TPFPB, the solubility of 1.5 wt%, 5 wt%, and 7.5 wt% of LiDFBP mixture in BE was achieved and no precipitation was observed, which meant the insoluble LiOTFP dissolved with the help of TPFPB.

To examine the dissolution properties of LiDFBP mixture with TPFPB, Nuclear Magnetic Resonance (NMR) spectroscopy was conducted using a single EMC solvent in order to simplify the analysis and more effectively demonstrate the changes in the solvation structure. Figs. 2a and S2 show that upon the addition of 1.5 wt% TPFPB to pure EMC, the ¹H chemical shifts of EMC molecules underwent various shifts towards lower magnetic field values to a different extent, indicating an increased deshielding effect. The H atoms bound to carbons close to C=O groups showed larger shifts (Fig. S2), which could be attributed to the enhanced electron-withdrawing inductive effect of the C=O groups in EMC molecules, indicating their participation in coordination with electron-withdrawing groups. Simultaneously, ¹⁹F chemical shift of TPFPB molecules, assigned to the three types of fluorine atoms on the benzene ring [51,52], shifted respectively, confirming the change of TPFPB coordination conditions (Fig. 2b). The electrostatic diagram obtained through DFT calculation revealed the impact of TPFPB on EMC.

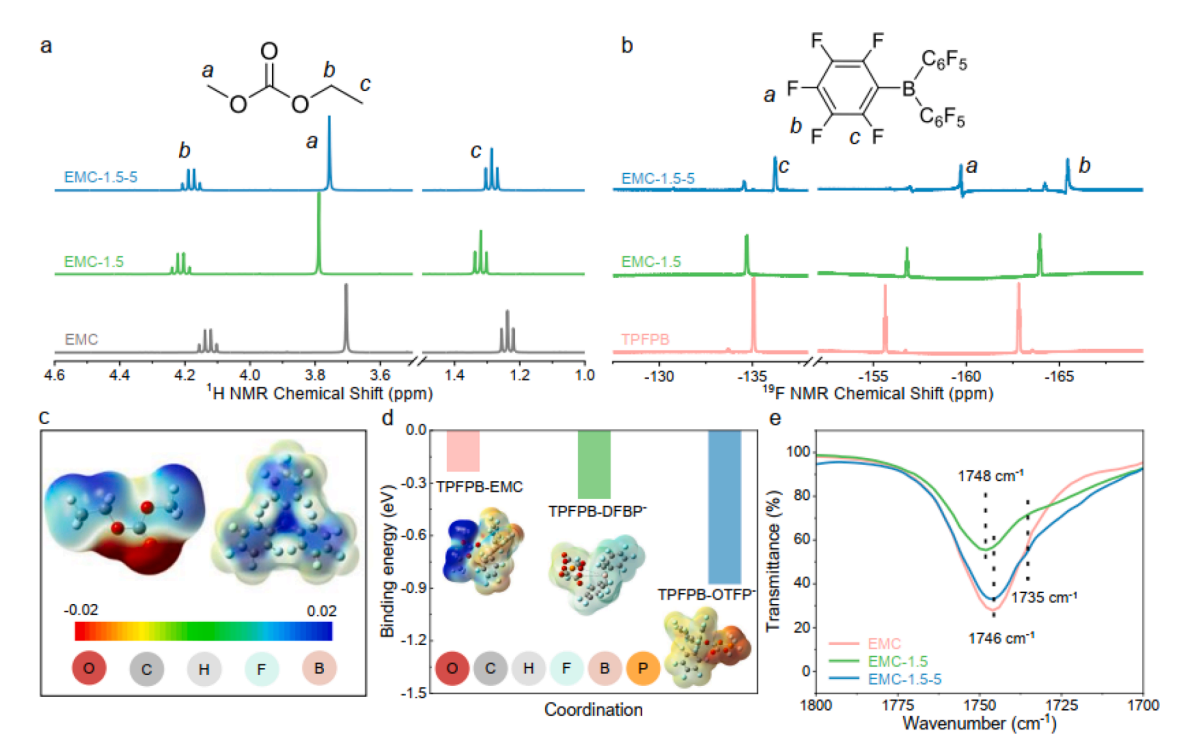


Fig. 2. The dissolution characteristics of LiDFBP mixture. (a) ¹H (b) ¹⁹F signals of pure EMC solvent, EMC-1.5 (EMC solution with 1.5 wt% TPFPB) and EMC-1.5–5 (EMC solution with 1.5 wt% TPFPB and 5 wt% LiDFBP mixtures), respectively. (c) The calculated electrostatic diagram of EMC and TPFPB molecular. (d) The calculated binding energy of TPFPB-EMC, TPFPB-DFBP⁻ and TPFPB-OTFP⁻. (e) The FTIR spectra of EMC, EMC-1.5 and EMC-1.5–5, respectively.

As shown in Fig. 2c, the electrostatic diagram clearly indicates that the C=O bond of EMC displayed stronger electronegativity, whereas the B atom of the TPFPB molecule exhibited the strongest electropositivity. These findings confirmed the potential coordination interactions existing between the -C=O and -B groups. Upon adding 5 wt% LiDFBP mixture to the EMC/TPFPB solution, the ¹H signals of EMC and ¹⁹F NMR signals of TPFPB shifted to higher fields simultaneously, indicating the preference of TPFPB to bind with DFBP or OTFP than EMC molecules. Fig. 2d illustrates that the coordination energy of TPFPB-OTFP (-0.8777 eV) and TPFPB-DFBP (-0.3844 eV) was lower than TPFPB-EMC (-0.2293 eV). This suggests that TPFPB tended to combine with OTFP or DFBP more than with EMC molecules.

Fourier transform infrared spectrometry (FTIR) was employed to investigate the coordination interactions between TPFPB and LiOTFP or LiDFBP. Fig. 2e shows that the peak at 1746 cm⁻¹, which was attributed to the C=O group of EMC[49], experienced a slight red-shift to 1748 cm⁻¹ upon the addition of 1.5 wt% TPFPB, due to the coordination interactions between EMC and TPFPB. Then, the introduction of 5 wt% LiDFBP mixture resulted in the binding of TPFPB molecules with OTFPor DFBP⁻ and EMC molecules were left as free molecules. Therefore, the FTIR peak of the C=O group returned to 1746 cm⁻¹. These findings offer insights into the mechanism that underlies the dissolution of LiDFBP mixture in pure EMC solvent, with the aid of TPFPB. To further investigate the dissolution characteristics of LiDFBP mixtures in real electrolyte systems, we obtained FTIR spectra of the baseline electrolyte (1.0 M LiPF₆ in EC/EMC/DMC=1/1/1 by volume) and the designed electrolyte (1.0 M LiPF₆ in EC/EMC/DMC=1/1/1 by volume with 1.5 wt % TPFPB and 5 wt% LiDFBP mixture), as presented in Fig. S3, which confirmed previous findings. In combination with the calculated atomic

charges of the components in this electrolyte system (Fig. S4), it can be concluded that extra OTFP⁻ can exist in the form of TPFPB-OTFP⁻. As a result, the solubility of LiOTFP could be notably enhanced.

3.2. The CEI generating ability of the electrolyte

The additive played a pivotal role in altering the physical properties of the base electrolyte (BE). By introducing TPFPB and LiDFBP mixtures in appropriate amounts, the electrolyte's conductivity increased as the concentration of lithium salts rose. However, excessive additives had the opposite effect, decreasing the electrolyte's conductivity. Fig. S5 shows that, among the tested combinations, the electrolyte with 1.5 wt% TPFPB and 5 wt% LiDFBP mixture exhibited the highest conductivity. Hence, we selected this electrolyte as the designed electrolyte (DE).

Fig. 3a presents the molecular structure of the potential species in the electrolyte, along with their corresponding highest occupied molecular orbital (HOMO) and lowest unoccupied molecular orbital (LUMO) energies. Notably, free OTFP⁻ or TPFPB-OTFP⁻ displayed the highest HOMO energy values among the species in the electrolyte, indicating their preference to decompose and form cathode-electrolyte interface CEI onto the cathode material surface. Fig. S6 displays the linear sweep voltammetry (LSV) curves of BE and DE. Interestingly, DE exhibited strong oxidation current around 4.3 V (vs. Li/Li⁺) and the magnified shot revealed that DE initiated decomposition at 3.5 V (vs. Li/Li⁺). This low oxidation resistance was a result of the presence of free OTFP⁻ or TPFPB-OTFP⁻, which preferentially forms CEI on the cathode surface, consistent with computational results. After two activation cycles at a current density of 0.2C (1C=200 mA g⁻¹), the SEM images in Fig. S7 displayed that while the surface of the LCO electrode in BE remained

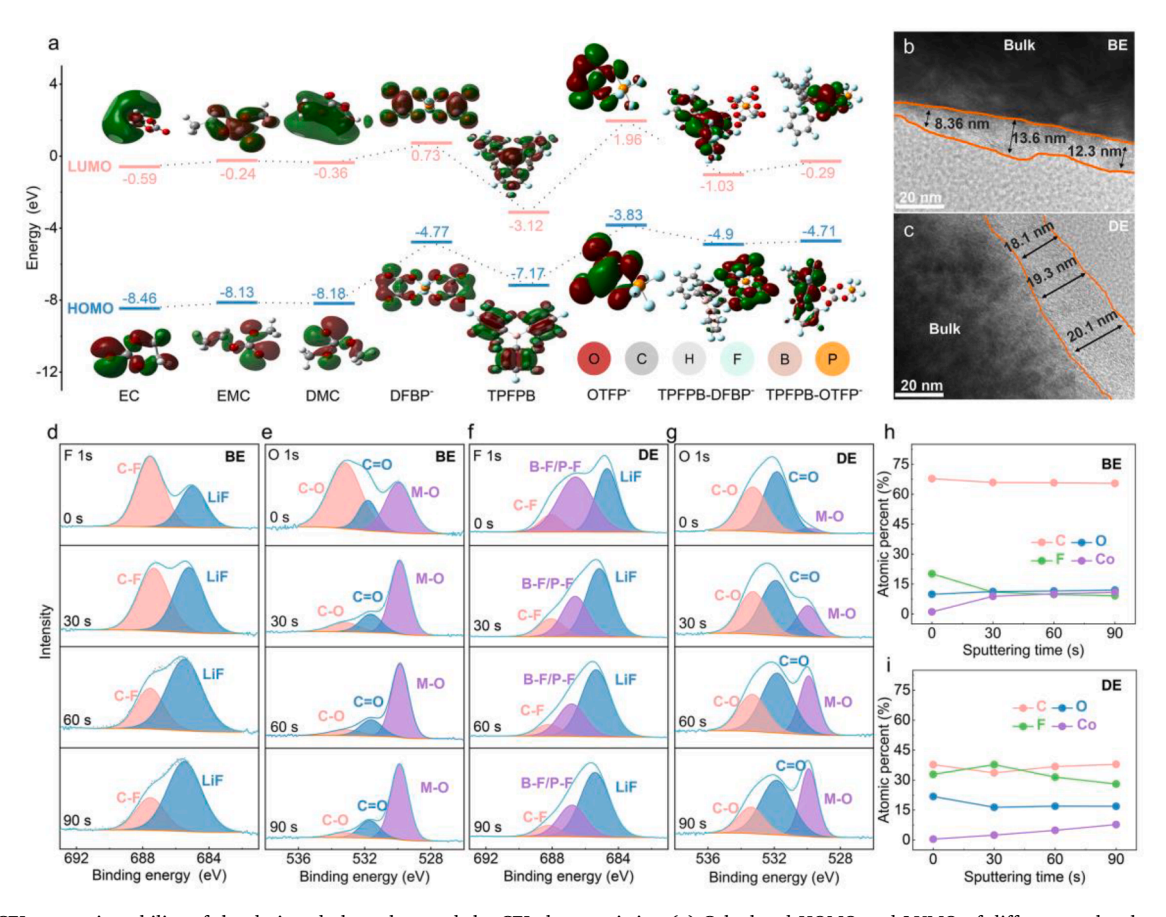


Fig. 3. The CEI generating ability of the designed electrolyte and the CEI characteristics. (a) Calculated HOMO and LUMO of different molecular. (b) The TEM images of LCO particles cycled in (c) BE and (d) DE after 50 cycles at 1C. (d) F 1s and (e) O 1s core spectra of LCO electrode surface after 50 cycles in BE at 1C. (f) F 1s, (g) O 1s and core spectra of LCO electrode surface after 50 cycles in DE at 1C. The atomic percent of C, F, O and Co elements changes with the sputtering time from 0 to 90 S of LCO electrolyte surface after 50 cycles at 1C in (h) BE and (i) DE.

smooth, a significant number of decomposition products appeared on the LCO surface in DE, demonstrating that DE had exceptional CEI formation capacity. Fig. 3b and c showed the high-resolution transmission electron microscopy (HR-TEM) images of LCO particles that were cycled in BE and DE after 50 cycles at a current density of 1C (200 mA g^{-1}). After being cycled in BE, the surface of LCO particles displayed uneven CEI film with thickness distributions that ranged from 8 to 14 nm approximately. In contrast, a more uniform CEI film with a thickness of roughly 19 nm was formed in DE. Additionally, through energy dispersive spectrometer (EDS) mapping of the two types of LCO particles cycled in different electrolytes (Figs. S8 and S9), an increased concentration of F element on the LCO surface after cycling in DE was observed. Furthermore, the Pt element (acting as a protective layer when prepared by the focused ion beam (FIB)) was even able to penetrate the BEinduced CEI and reach the LCO surface, while the DE-induced CEI exhibited a high dense and smooth surface, illustrating the superior CEI formation ability of DE. These findings demonstrated that DE is inclined to produce thick and uniform CEI layers that can help maintain the cycling stability of LCO under high-voltage circumstances, which will be discussed later.

XPS was performed to investigate the CEI properties on the LCO surface. The F 1s core spectra in BE (Fig. 3d) showed that the intensity of LiF (685.5 eV) [53,54] increased with the increase of sputtering time, while the content of C-F bonds (687.6 eV) decreased, indicating that LiF was more likely to appear in the inner layer of CEI. For the O 1s spectra (Fig. 3e), the contents of C—O (533.2 eV) and C=O bonds (531.6 eV) decreased with the increase of etched depth, while the content of M-O bonds (529.9 eV) [44], represented Co-O bonds in this system, which was ascribed to the dissolved Co³⁺ and bulk LiCoO₂) increased. The contents change of corresponding bonds of LCO surface in DE showed the same trend. However, the F 1s XPS spectra (Fig. 3f) revealed that the LiF content in DE was higher than that in BE, which could effectively stabilize the CEI. In addition, the B-F/P-F bonds (686.6 eV) [55,56] appeared in the LCO surface in DE, which was almost ascribed to the composition of TPFPB-OTFP species and played an important role in stabilizing CEI. Furthermore, as shown in Fig. 3g, fewer M-O bonds were contained in the LCO surface in DE, especially without sputtering, indicating less Co³⁺ dissolution. In addition, the LCO surface in DE also contained P-O bonds (134.4 eV) and P-M bonds (130.2 eV, which was ascribed to P-Co bonds in this system, Fig. S10a) [57,58], while P elements appeared only when there was no sputtering on LCO surface in BE (Fig. S10b). Apparently, in the absence of sputtering, there was no M-O bonds in LCO surface in DE, indicating that the P element could bind to the Co³⁺ to be dissolved, inhibiting the dissolution of Co³⁺. In addition, the B element produced by TPFPB-OTFP decomposition further stabilized the CEI of DE (Fig. S11). Fig. 3h and i also show the atomic ratio of C, F, O and Co elements in LCO surface with BE and DE. Obviously, more F element emerged in the CEI derived from DE, especially with sputtering, approximately 3 times that of BE. Specifically, irrespective of the duration of etching, the content ratio of LiF in DE-induced CEI was consistently higher than that of BE. Furthermore, the presence of B-F/P-F bonds resulted in less than 10% of the C-F bond being detected in the DE-induced CEI following 90 s of sputtering. This value accounted for only about a quarter of the BE-induced CEI (Fig. S12). The SEM-EDS mapping of the LCO electrodes after 50 cycles also confirms the presence of a higher amount of fluorine (F) element on the surface of LCO electrode after being cycled in DE, as shown in Figs. S13 and S14. It can be safe to conclude that there were more inorganic components in DE induced CEI, enabling the excellent stability. The C 1s spectra also confirmed that there was more compact and thicker CEI formed on LCO surface in DE from the less content of C-F bonds (290.0 eV) [37,38] at the LCO surface without sputtering (Fig. S15).

3.3. The phase transformations of LCO surface

During the charging process at a high cut-off voltage, the crystal

structure of LCO particles is altered from a layered phase to a spinel phase [4]. Next, the spinel phase switches to a rock-salt phase, which results in the dissolution of Co³⁺ and the breakdown of the LCO surface lattice structure, causing the failure of the LCO cathode [5]. The formation of high-resistance CEI on LCO surfaces had an impactful role in the transformation of LCO's phase. The CV profiles of LCO cycled in BE and DE are presented in Figs. 4a and S11. For DE, LCO showed a unique first charge curve where only a weak current density was observed from about 4.0 to 4.54 V (vs. Li/Li⁺). These findings indicated the transfer of Li ions from LCO to bulk electrolyte were inhibited during the first few cycles. Beyond 4.54 V (vs. Li/Li⁺), the current density increased sharply, which could be ascribed to the formation of lithium-ion transport channels inside the CEI layer. Notably, even if reverse scanning of the CV curve began, the oxidation current (other than the reduction current) continued to increase, demonstrating the presence of a high local over-potential existed on the LCO particle surface. Meanwhile, a new reduction peak appeared at ~3.58 V (vs. Li/Li⁺), indicating the formation of a spinel phase. These findings were also observed in galvanostatic charge/discharge profiles (Fig. 4b). This can be attributed to the formation of a high-resistance CEI layer on the outer surface of LCO, inhibiting the fast transfer of Li ions from LCO to bulk electrolyte. Once the constant current charging was initiated, the voltage immediately reached above 4.55 V (vs. Li/Li⁺), resulting in the significant increase of the local overpotential on the LCO surface. As a consequence, the outer surface of LCO underwent a phase transformation from the layered phase to the spinel phase first, due to the voltage rising beyond 4.55 V (vs. Li/Li⁺). A discharge platform corresponding to the spinel phase occurred around 3.6 V (vs. Li/Li⁺). Ex-suit Raman spectroscopy demonstrated the presence of spinel layer, with the new peak around $520.9~\text{cm}^{-1}$ corresponding to the F_{2g} Raman-active mode of Co_3O_4 structure (Fig. 4c) [59-61]. To reveal the effect of the by-product LiOTFP, a new electrolyte was formulated, consisting solely of BE with 1.5 wt% TPFPB and 5 wt% pure LiDFBP (LiDFBP in EMC solvent), as opposed to the 5 wt% LiDFBP mixtures previously employed. Figs. S16a and S16b indicate the absence of voltage changes in the range of 4.0–4.54 V (vs. Li/Li⁺) or a CV reduction peak at approximately 3.58 V (vs. Li/Li⁺) during the initial cycle, which is indicative of spinel phase formation on the LCO surface. Thus, it is reasonable to conclude that LiOTFP, as the key component in the DE system, undergoes preferential oxidation to generate a dense CEI layer and further stabilize the spinel phase on the LCO surface during activation cycles. As the result, the electrolyte composed of BE with 1.5 wt% TPFPB and 5 wt% pure LiDFBP exhibited reduced cycling stability but improved rate performance when compared to that of DE (Fig. S16c and d). Fig. 4d presents the HR-TEM pattern of the LCO particle after cycling in BE, revealing a dissolved layer was clearly visible, implying that BE cannot effectively prevent the collapse of the surface structure of LCO under high voltage. In contrast, Fig. 4e displays a dense spinel layer with a thickness of roughly 2 nm formed on the LCO surface after cycling in DE without any observable dissolved LCO phases. The incorporated FTT pattern in the inset of the selected region of LCO confirmed the presence of a thin and condensed spinel layer [26]. These results indicated that the rapid formation of a dense CEI during the initial few cycles prevented the Co^{3+} dissolution and the phase transition of LCO surface, which led to the development of a thin spinel layer. As a result, a protective bilayer consisting of a LiF-rich cathode-electrolyte interphase (CEI) as the outermost layer and a layer of spinel structure as the inner layer was established in situ on the LCO particles.

The in-suit constructed protective bilayer, featuring a thin inner spinel layer and a dense outer CEI, effectively prevents the irreversible transition of bulk phase and Co³⁺ dissolution. Concentrations of dissolved Co on the separators of Li||LCO half-cells after certain cycles with different electrolytes were measured using an inductively coupled plasma atomic emission spectrometer (ICP-AES), as seen in Fig. 4f. Clearly, lower concentrations of dissolved Co were detectable after certain cycles in DE, indicating the good stability of LCO structure after

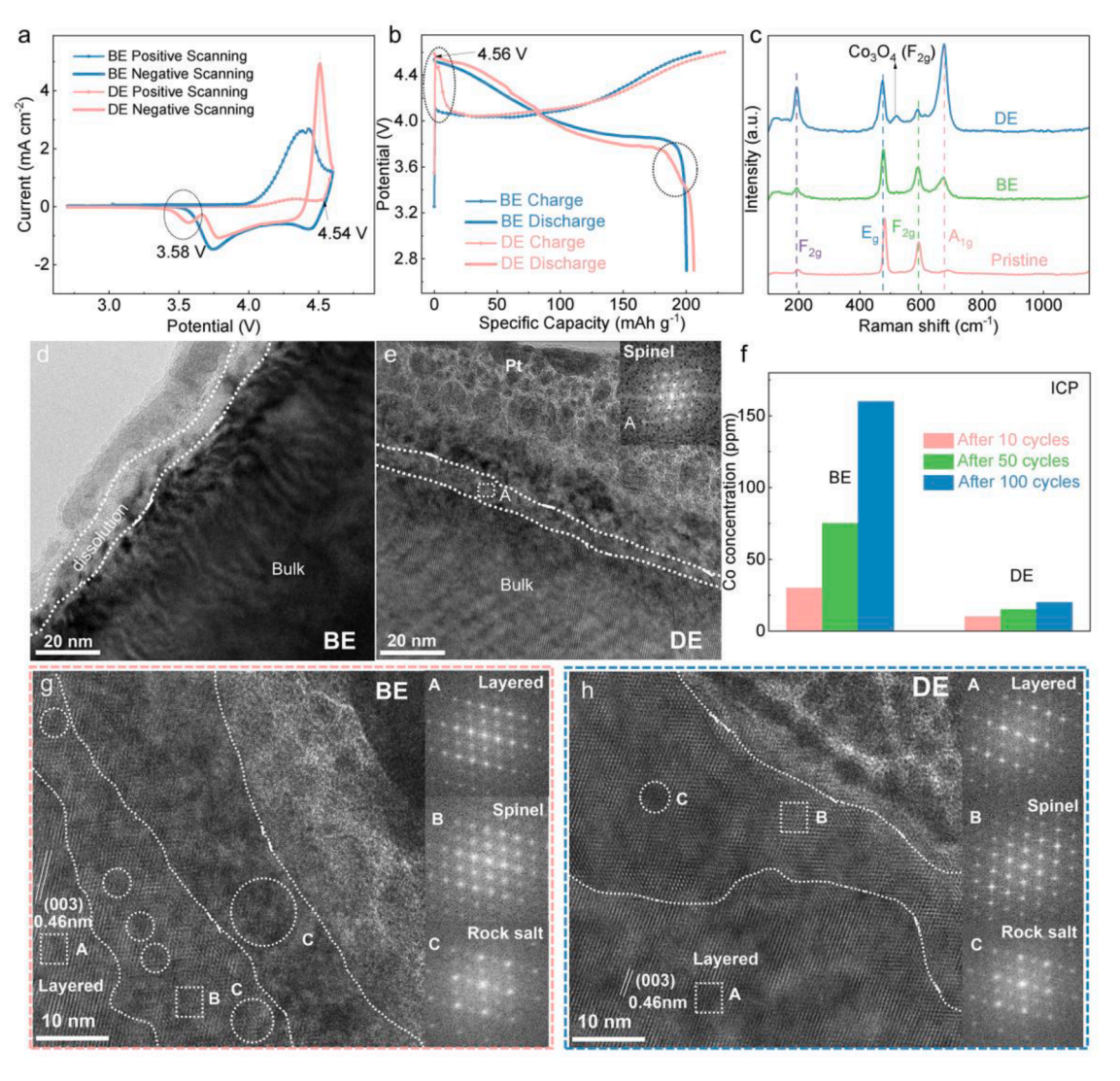


Fig. 4. The phase transformations of LCO electrode in different electrolytes. (a) CV profiles and (b) galvanostatic charge/discharge profiles at the first cycle of Li|| LCO half-cells in BE and DE, respectively. (c) The Raman spectra of pristine LCO electrode and the LCO electrodes after 10 cycles in BE and DE. The TEM image of LCO particle after 2 cycles in (d) BE and (e) DE with the current density of 0.2 C. (f) The contents of transition metal Co ions in different electrolytes after certain cycles. The HR-TEM images of LCO particles after 200 cycles under the operation voltage between 2.7 and 4.6 V (vs. Li/Li⁺) in (g) BE and (h) DE and the corresponding FTT patterns.

100 cycles. This can be attributed to the formation of a high impedance CEI during the first cycle, which induces phase transformation on the surfaces of LCO and forms a stable spinel phase, thereby preventing Co dissolution. To further investigate the phase transformation of LCO particles, HR-TEM analysis was conducted after 200 cycles at 1C between 2.7 and 4.6 V (vs. Li/Li⁺). Fig. 4g displays that after cycling in BE, a thick rock-salt phase and a mixed phase with numerous rock-salt region doped in the spinel phase were generated from the outer layer to the inside layer, which can be confirmed by the FTT patterns of the selected regions. This suggested that BE could not suppress the irreversible phase transformation of LCO particles, as previously reported. However, upon cycling in DE, merely a mixed layer comprising a small amount of rock-salt phase and a higher fraction of spinel phase appeared at the outermost layer, and a significantly thicker layered phase was observed on the LCO surface (Fig. 4h). According to the EDS line scan data (Fig. S17), the elemental distribution along the depth reveals that the intensity ratio between Co and O elements at the surface of the LCO particle significantly increased after 200 cycles in DE. In contrast, no change in ratio was observed on the LCO surface cycled in BE, with only a decreasing trend for both elements. Thus, it confirms that, the dense Co₃O₄ structure formed in DE-induced LCO surface rather thanLi_xCoO₂-

type spinel-like surface, which stabilized the bulk crystal structures of LCO. In BE, the lack of a dense CEI and spinel phase caused the LCO surface to be highly unstable, resulting in the continual collapse of its layered structure and eventual dissolution into the electrolyte. This further confirmed that the protective bilayers greatly suppressed the irreversible phase transformation of bulk LCO during long cycles.

To further investigate the effect of the designed electrolyte on structural deformation of LCO particles, in-suit Raman spectra analysis was carried out. Fig. 5a shows two characteristic peaks at 485 and 595 cm $^{-1}$, corresponding to variations in the O—Co-O bending (Eg) and Co-O stretching (A1g) of LCO, respectively [59]. During the charging process, the LCO samples in both BE and DE exhibited similar trends. The intensity of Eg and A1g peaks in BE and DE decreased, indicating the weakening of the O—Co-O and Co-O bonds under high voltage [10]. However, BE did not show the corresponding peaks during the discharging process, but the corresponding peaks in DE gradually recovered. Fig. 5b shows the Raman spectra at OCP, charged to 4.6 V (vs. Li/Li $^{\rm +}$) and discharged to 3.0 V (vs. Li/Li $^{\rm +}$). As confirmed by previous analysis, the phase transformation process of LCO particles in DE was more reversible, and the spinel phase appeared when the LCO electrode was discharged to 3.0 V (vs. Li/Li $^{\rm +}$). This was contributed to the superior

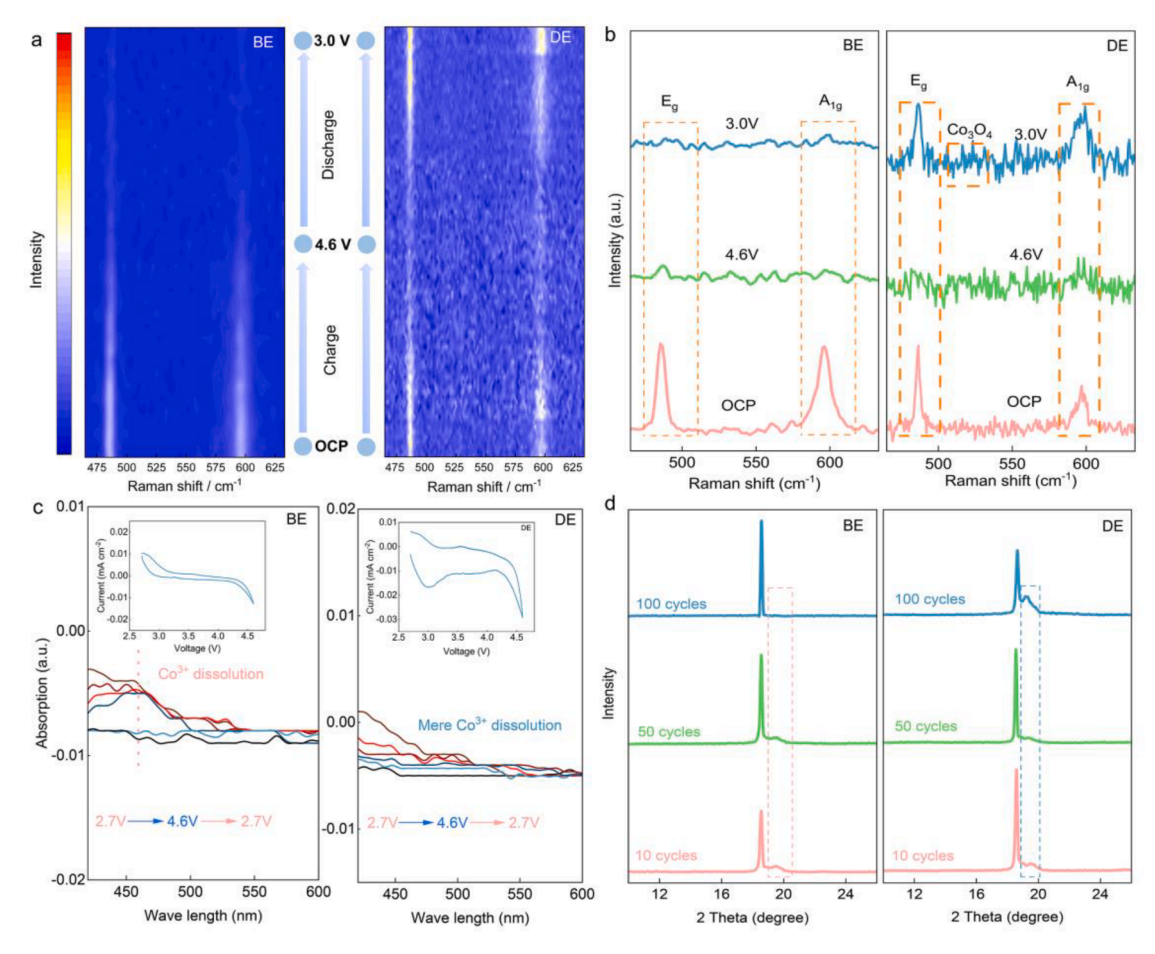


Fig. 5. Structural and phase transformation analysis of LCO in different electrolytes. (a) In-situ Raman spectra evolution of the LCO particles in BE and DE at the E_g and A_{1g} Raman active vibrational peaks during the first cycle at 0.5 mV s⁻¹. (b) The selected Raman spectra at different states of charge and discharge. (c) In-suit UV spectra of Co^{3+} ions in BE and DE during the first cycle and the corresponding CV profiles are depicted in the inset. (d) The XRD patterns of LCO electrodes cycled in BE and DE charged to 4.6 V (vs. Li/Li⁺) after different cycles at a current of 200 mA g^{-1} .

interaction between the dense CEI and LCO surface, as well as the spinel layer on the outer surface of LCO, prohibiting significant structural degradation during high voltage cycling. The irreversible phase transformation always generated ${\rm Co}^{3+}$ dissolution during the cycling process. Therefore, the *in-situ* Ultraviolet and Visible (UV) spectrum was performed to investigate the distinct ${\rm Co}^{3+}$ dissolution features at the first cycle with BE and DE. As shown in Fig. 5c, obvious characteristic peak around 470 nm attributed to ${\rm Co}^{3+}$ could be found after cycled in BE while there was no apparent peak emerged in DE [62]. The difference once again indicated the significant effect of DE in prohibiting the LCO's irreversible phase transformation under high voltage operation.

XRD patterns of LCO electrodes after cycles were performed to investigate the phase transformation reversibility of LCO in both BE and DE which was charged to 4.6 V (vs. Li/Li⁺) after different cycles (Figs. 5d and S18). After 10 and 50 cycles, two peaks assigned to the O3 and H1-3 phases at 18.4° and 19.3° [63], respectively, were observed in both electrolytes. The small peak at 19.3° of LCO electrodes in BE disappeared after 100 cycles, while it became shaper in DE. Consequently, the results indicated that the LCO cathode has poor H1-3 phase transfer ability after cycling in BE, while displaying satisfactory phase transformation reversibility in DE. This finding highlights the significance of the protective bilayers, comprising a dense CEI and a thin spinel layer of LCO, that significantly enhances the structural stability of LCO under high voltage.

3.4. Electrochemical performance

The cycling stability of the LCO cathode was investigated at a 4.6 V (vs. Li/Li $^+$) cut-off charge voltage using Li||LCO half-cells. Fig. 6a shows that the LCO cathode displayed a high reversible discharge capacity of approximately 207 mAh g $^{-1}$ at 0.2C (1C =200 mA g $^{-1}$). Remarkably, the capacity retention of 80.1% and 51.2% (in comparison with the third cycle) was attained following 400 and 1000 cycles at 1C in DE respectively. In contrast, the LCO electrode that cycled in BE degraded to 2% after 400 cycles. Moreover, the average coulombic efficiency (CE) of DE was 99.8% during 1000 cycles, significantly higher than that in BE. This could be attributed to the protective bilayer formation, which hindered the continuous electrolyte decomposition and the Co $^{3+}$ dissolution on the LCO surface.

Graphite||LCO pouch cells were assembled to investigate the practicality of this electrolyte system. Fig. 6b illustrates the galvanostatic charge/discharge profiles of the punch cell using BE over various cycles, with a voltage range of 3–4.55 V (vs. Li/Li⁺) at 1C (1C=620 mA). The pouch cell with BE delivered an initial reversible capacity of 623 mAh with an initial coulombic efficiency of 98.1%. However, it exhibited severe capacity fading, with only 31.3% retention after 500 cycles. In contrast, the pouch cell using DE exhibited good cycling stability, experiencing only a slight capacity decay and retaining 97.7% capacity after 500 cycles as shown in Fig. 6c. Nevertheless, the initial reversible capacity was only 539 mAh, with an initial coulombic efficiency of 97.6%, which was considerably lower than the corresponding value in BE. The reason for this can be ascribed to the interface's high resistance

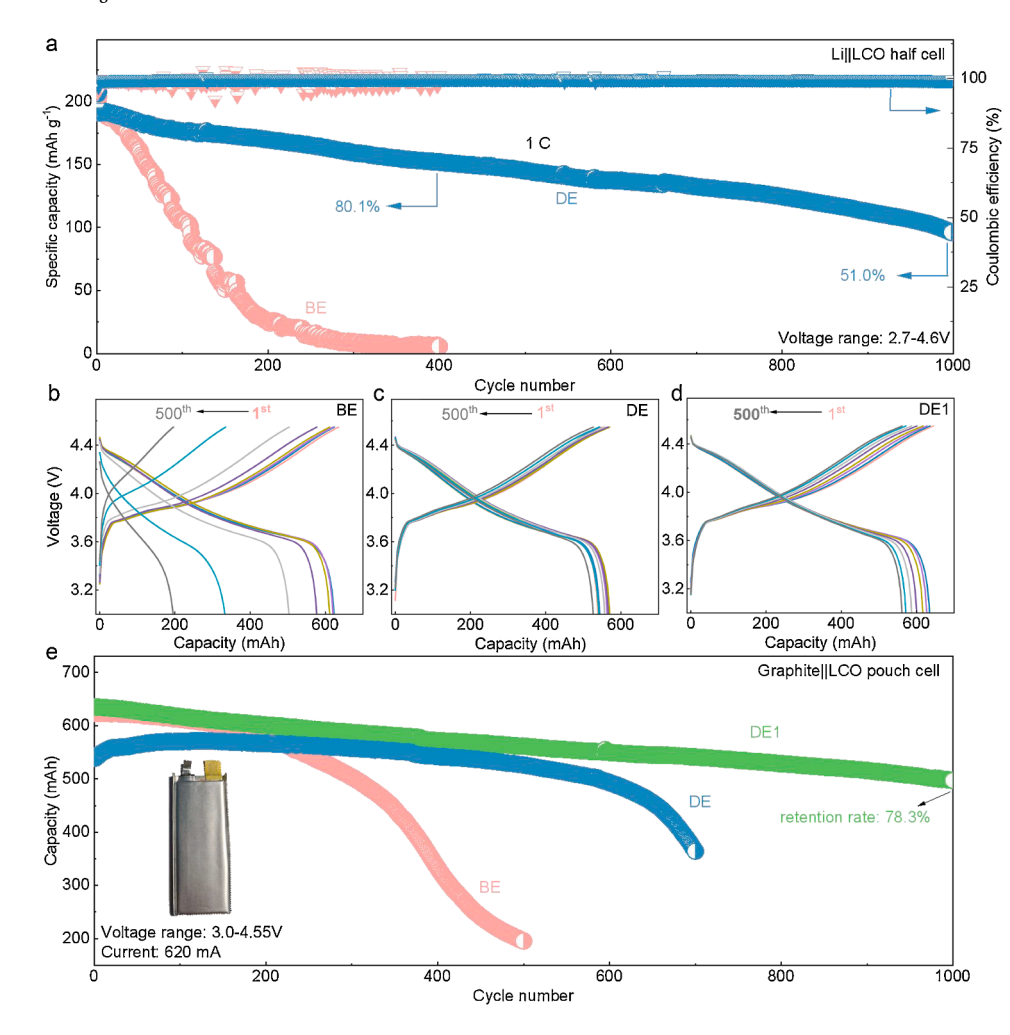


Fig. 6. The electrochemical performance of different electrolytes. (a) The cycling performance of LCO cathodes in BE and DE with the voltage range from 2.7 to 4.6 V (vs. Li/Li⁺) at 1C (1C = 200 mA g⁻¹) after 2 activation cycles at 0.2C and areal mass loading of 6.8 mg cm⁻² in Li||LCO half-cells. Galvanostatic charge/discharge profiles of graphite||LCO pouch cells with different cycles at 1C (1C=620 mA) in (b) BE, (c) DE and (d) DE1 electrolyte, respectively. (e) The cycling performance of graphite||LCO pouch cells with different electrolytes at the current density of 1C.

of CEI and SEI on cathode or anode [64,65]. Fig. S19 illustrates that the R_{CEI} of Li||LCO cells with DE was higher than that with BE due to the thicker CEI and the presence of the spinel phase. The LCO half-cell using DE delivered slightly reduced capacities and significantly increased cycling stability at various C rates (Figs. S20 and S21). Similar findings were observed in Li||graphite half cells (Figure S22). In contrast to BE, the Li||graphite cell in DE displayed a slow activation process, notwithstanding its remarkable long cycling stability (Fig. S23). This was primarily due to the formation of a high-resistance SEI on the graphite anodes.

A new electrolyte, designated as DE1, was developed to mitigate these effects by incorporating 0.5 wt% TPFPB and 1.5 wt% LiDFBP mixture in BE and optimizing its application in pouch cells. The graphite||LCO pouch cell utilizing DE1 exhibited a superior initial capacity of 635 mAh at 1C, with the initial CE of the pouch cells escalating to 98.5%. Although there was slow capacity fading in the electrode, it still achieved a capacity retention of 88.5% even after 500 cycles (Fig. 6d). The cycling mean voltage of the pouch cells containing the three different electrolytes was depicted in Fig. S24. Compared to the BE, both DE and DE1 exhibited a higher mean operation voltage, indicating the boosted reversibility of the LCO structure in DE and DE1. The highest operation voltage in DE1 suggests that the optimized compositions could enable a high capacity retention rate while preserving the available reversible capacity, unlike DE. The pouch cell with BE had a high swollen ratio, rising up to 54.9% after 500 cycles (Fig. S25), due to severe side-reactions. However, the swollen ratio decreased significantly to 8.3% and 1.5% in DE and DE1, respectively. This finding indicates that both electrolytes inhibited the decomposition of electrolytes and

the potential lithium plating. As a result, the average efficiency of DE and DE1 remained as high as 99.9%, exceeding BE's 99.8% in the first 500 cycles (Fig. S26). The long-term cycling performance of the pouch cells containing BE, DE, and DE1 was illustrated in Fig. 6e. The cell with BE exhibited quick failure after only 300 cycles, while DE demonstrated significantly increased cycling stability due to the protective bilayers on the LCO surface. However, capacity fading still occurred suddenly after about 600 cycles, primarily due to Li plating on graphite owing to the high resistance SEI. As depicted in Fig. S27, partial Li plating was evident on the graphite electrode after cycles with DE, while the graphite was almost entirely coated with plated Li after only 500 cycles with BE. In contrast, the optimized DE1 showed cathode stability and good resistance to Li plating on the graphite anode. Therefore, the pouch cell utilizing DE1 delivered a 78.9% capacity retention even after 1000 cycles under the operation voltage windows of 3.0–4.55 V (vs. Li/Li⁺).

4. Conclusion

The production processes of solid-phase LiDFBP are always accompanied by impurities, including LiOTFP. A further purification process not only increases production cost but also causes material waste. This study demonstrated that a LiDFBP mixture containing LiOTFP could be directly used in a carbonate-based electrolyte through employing TPFPB as the electron receptor. The optimized electrolyte thus obtained could achieve high cycling stability of high voltage LCO. By using NMR, FTIR, and DFT calculations, the dissolution characteristics of LiOTFP in a carbonate-based electrolyte were investigated. Our findings showed that a protective bilayer was constructed *in-situ*, consisting of a compact

cathode electrolyte interface (CEI) and a dense spinel layer on the LCO cathode surface, which effectively prevented the irreversible phase transformation of LCO under high voltage. Consequently, the Li||LCO half-cells demonstrated 80.1% and 51.0% specific capacity retention after 400 and 1000 cycles, respectively, at 1C under 4.6 V (vs. Li/Li $^{\rm +}$) cut-off charge voltage. The capacity retention of the graphite||LCO pouch cell using the optimized electrolyte reached 78.9% after 1000 cycles at 1C, with the voltage range from 3.0 to 4.55 V (vs. Li/Li $^{\rm +}$). Our research establishes an effective and economical approach to enhance the energy density of lithium-ion batteries (LIBs).

CRediT authorship contribution statement

Hao Zhang: Conceptualization, Methodology, Writing – original draft. Yuxiang Huang: Data curation. Yue Wang: Data curation. Lu Wang: Data curation. Zhibo Song: Data curation. Haoliang Wang: Data curation. Caixia Xu: Data curation. Xingtao Tian: Data curation. Siyu Wang: Data curation. Jianjun Fang: Data curation. Wenguang Zhao: Data curation. Hongbin Cao: Data curation. Xiangming Yao: Data curation. Jie Yang: Data curation. Rui Tan: Data curation. Luyi Yang: Supervision, Funding acquisition, Project administration. Yan Zhao: Conceptualization, Methodology, Writing – review & editing, Supervision, Funding acquisition.

Declaration of Competing Interest

The authors declare that they have no known competing financial interests or personal relationships that could have appeared to influence the work reported in this paper.

Data availability

Data will be made available on request.

Acknowledgments

This work was kindly supported by Special Appointment Position Project C of Shenzhen Pengcheng Peacock Plan (No. 1270110333), Basic and Applied Basic Research Foundation of Guangdong Province (No. 2021B1515130002), The Shenzhen Science and Technology Research Grant (No. JCYJ20200109140416788), Soft Science Research Project of Guangdong Province (No. 2017B030301013), and Shenzhen Science and Technology Research Grant (No. ZDSYS201707281026184).

Supplementary materials

Supplementary material associated with this article can be found, in the online version, at doi:10.1016/j.ensm.2023.102951.

References

- [1] T. Fujita, K. Toda, Microdisplacement measurement using a liquid-delay-line oscillator, Jpn. J. Appl. Phys. Part 1 Regul. Pap. Short Notes Rev. Pap. 42 (2003) 6131–6134, https://doi.org/10.1143/jjap.42.6131.
- [2] M.S. Whittingham, Lithium batteries and cathode materials, Chem. Rev. 104 (2004) 4271–4301, https://doi.org/10.1021/cr020731c.
- [3] S. Yang, R. He, Z. Zhang, Y. Cao, X. Gao, X. Liu, CHAIN: cyber hierarchy and interactional network enabling digital solution for battery full-lifespan management, Matter 3 (2020) 27–41, https://doi.org/10.1016/j. matt.2020.04.015.
- [4] S.D. Zhang, M.Y. Qi, S.J. Guo, Y.G. Sun, X.X. Tan, P.Z. Ma, J.Y. Li, R.Z. Yuan, A. M. Cao, L.J. Wan, Advancing to 4.6V review and prospect in developing high-energy-density LiCoO₂ cathode for lithium-ion batteries, Small Methods 6 (2022) 1–17, https://doi.org/10.1002/smtd.202200148.
- [5] Y. Lyu, X. Wu, K. Wang, Z. Feng, T. Cheng, Y. Liu, M. Wang, R. Chen, L. Xu, J. Zhou, Y. Lu, B. Guo, An overview on the advances of LiCoO₂ cathodes for lithium-ion batteries, Adv. Energy Mater. 11 (2021) 1–29, https://doi.org/10.1002/aenm.202000982.

- [6] A. Manthiram, A reflection on lithium-ion battery cathode chemistry, Nat. Commun. 11 (2020) 1–9, https://doi.org/10.1038/s41467-020-15355-0.
- [7] W. Liu, J. Li, W. Li, H. Xu, C. Zhang, X. Qiu, Inhibition of transition metals dissolution in cobalt-free cathode with ultrathin robust interphase in concentrated electrolyte, Nat. Commun. 11 (2020), https://doi.org/10.1038/s41467-020-17396-x
- [8] M.D. Radin, S. Hy, M. Sina, C. Fang, H. Liu, J. Vinckeviciute, M. Zhang, M. S. Whittingham, Y.S. Meng, A. Van der Ven, Narrowing the gap between theoretical and practical capacities in Li-ion layered oxide cathode materials, Adv. Energy Mater. 7 (2017) 1–33, https://doi.org/10.1002/aenm.201602888.
- [9] J. Langdon, A. Manthiram, A perspective on single-crystal layered oxide cathodes for lithium-ion batteries, Energy Storage Mater. 37 (2021) 143–160, https://doi. org/10.1016/j.ensm.2021.02.003
- [10] H. Huang, Z. Li, S. Gu, J. Bian, Y. Li, J. Chen, K. Liao, Q. Gan, Y. Wang, S. Wu, Z. Wang, W. Luo, R. Hao, Z. Wang, G. Wang, Z. Lu, Dextran sulfate lithium as versatile binder to stabilize high-voltage LiCoO₂ to 4.6V, Adv. Energy Mater. 11 (2021), https://doi.org/10.1002/aenm.202101864.
- [11] Q. Zhang, J. Pan, P. Lu, Z. Liu, M.W. Verbrugge, B.W. Sheldon, Y.T. Cheng, Y. Qi, X. Xiao, Synergetic effects of inorganic components in solid electrolyte interphase on high cycle efficiency of lithium ion batteries, Nano Lett. 16 (2016) 2011–2016, https://doi.org/10.1021/acs.nanolett.5b05283.
- [12] J. Li, Y. Ji, H. Song, S. Chen, S. Ding, B. Zhang, L. Yang, Y. Song, F. Pan, Insights into the interfacial degradation of high-voltage all-solid-state lithium batteries, Nano Micro Lett. 14 (2022) 1–13, https://doi.org/10.1007/s40820-022-00936-z.
- [13] G.G. Amatucci, J.M. Tarascon, L.C. Klein, Cobalt dissolution in LiCoO₂-based non-aqueous rechargeable batteries, Solid State Ion. 83 (1996) 167–173, https://doi.org/10.1016/0167-2738(95)00231-6.
- [14] W. Xue, R. Gao, Z. Shi, X. Xiao, W. Zhang, Y. Zhang, Y.G. Zhu, I. Waluyo, Y. Li, M. R. Hill, Z. Zhu, S. Li, O. Kuznetsov, Y. Zhang, W.K. Lee, A. Hunt, A. Harutyunyan, Y. Shao-Horn, J.A. Johnson, J. Li, Stabilizing electrode-electrolyte interfaces to realize high-voltage Li||LiCoO2batteries by a sulfonamide-based electrolyte, Energy Environ. Sci. 14 (2021) 6030–6040, https://doi.org/10.1039/d1ee01265g.
- [15] Y. Xu, E. Hu, K. Zhang, X. Wang, V. Borzenets, Z. Sun, P. Pianetta, X. Yu, Y. Liu, X. Q. Yang, H. Li, *In situ* visualization of state-of-charge heterogeneity within a LiCoO₂ particle that evolves upon cycling at different rates, ACS Energy Lett. 2 (2017) 1240–1245. https://doi.org/10.1021/acsenergylett.7b00263.
- [16] J. Li, C. Lin, M. Weng, Y. Qiu, P. Chen, K. Yang, W. Huang, Y. Hong, J. Li, M. Zhang, C. Dong, W. Zhao, Z. Xu, X. Wang, K. Xu, J. Sun, F. Pan, Structural origin of the high-voltage instability of lithium cobalt oxide, Nat. Nanotechnol. 16 (2021) 599–605, https://doi.org/10.1038/s41565-021-00855-x.
- [17] K. Wang, J. Wan, Y. Xiang, J. Zhu, Q. Leng, M. Wang, L. Xu, Y. Yang, Recent advances and historical developments of high voltage lithium cobalt oxide materials for rechargeable Li-ion batteries, J. Power Sources 460 (2020), 228062, https://doi.org/10.1016/j.jpowsour.2020.228062.
- [18] A. Jena, P.H. Lee, W.K. Pang, K.C. Hsiao, V.K. Peterson, T. Darwish, N. Yepuri, S. H. Wu, H. Chang, R.S. Liu, Monitoring the phase evolution in LiCoO₂ electrodes during battery cycles using *in-situ* neutron diffraction technique, J. Chin. Chem. Soc. 67 (2020) 344–352, https://doi.org/10.1002/jccs.201900448.
- [19] L. Wang, B. Chen, J. Ma, G. Cui, L. Chen, Reviving lithium cobalt oxide-based lithium secondary batteries-toward a higher energy density, Chem. Soc. Rev. 47 (2018) 6505–6602, https://doi.org/10.1039/c8cs00322j.
- [20] A. Li, X. Cao, Y. Yang, J. Borovilas, D. Huang, C. Wang, X. Chuan, A strategy to stabilize 4 V-class cathode with ether-containing electrolytes in lithium metal batteries, J. Power Sources 440 (2019), 227101, https://doi.org/10.1016/j. ipowsour.2019.227101.
- [21] C. Julien, S. Gastro-Garcia, Lithiated cobaltates for lithium-ion batteries: structure, morphology and electrochemistry of oxides grown by solid-state reaction, wet chemistry and film deposition, J. Power Sources 97–98 (2001) 290–293, https://doi.org/10.1016/S0378-7753(01)00676-0.
- [22] T. Wu, Y. Zhao, X. Zhang, S. Ma, K. Wei, Y. Wei, Y. Cui, Improved solid interfacial kinetics and electrochemical performance for LiCoO₂(1 1 0) textured thin-film lithium batteries, Appl. Surf. Sci. 591 (2022), 153174, https://doi.org/10.1016/j. apsusc.2022.153174.
- [23] Y. Pei, C.Y. Xu, Y.C. Xiao, Q. Chen, B. Huang, B. Li, S. Li, L. Zhen, G. Cao, Phase transition induced synthesis of layered/spinel heterostructure with enhanced electrochemical properties, Adv. Funct. Mater. 27 (2017), https://doi.org/ 10.1002/adfm.201604349.
- [24] G.K. Mishra, M. Gautam, S. Sau, S. Mitra, Surface-modified lithium cobalt oxide (LiCoO₂) with enhanced performance at higher rates through Li-vacancy ordering in the monoclinic phase, ACS Appl. Energy Mater. 4 (2021) 14260–14272, https:// doi.org/10.1021/acsaem.1c02993.
- [25] W. Huang, Q. Zhao, M. Zhang, S. Xu, H. Xue, C. Zhu, J. Fang, W. Zhao, G. Ren, R. Qin, Q. Zhao, H. Chen, F. Pan, Surface design with cation and anion dual gradient stabilizes high-voltage LiCoO₂, Adv. Energy Mater. 12 (2022) 1–10, https://doi.org/10.1002/aenm.202200813.
- [26] S. Song, Y. Li, K. Yang, Z. Chen, J. Liu, R. Qi, Z. Li, C. Zuo, W. Zhao, N. Yang, M. Zhang, F. Pan, Interplay between multiple doping elements in high-voltage LiCoO₂, J. Mater. Chem. A 9 (2021) 5702–5710, https://doi.org/10.1039/d0ta09931e.
- [27] J.H. Shim, K.S. Lee, A. Missyul, J. Lee, B. Linn, E.C. Lee, S. Lee, Characterization of spinel LixCo₂O₄-coated LiCoO₂ prepared with post-thermal treatment as a cathode material for lithium ion batteries, Chem. Mater. 27 (2015) 3273–3279, https://doi. org/10.1021/acs.chemmater.5b00159.
- [28] J. Wei, Y. Ji, D. Liang, B. Chen, C. Jiang, X. Li, Anticorrosive nanosized LiF thin film coating for achieving long-cycling stability of LiCoO₂ at high voltages, Ceram. Int. 48 (2022) 10288–10298, https://doi.org/10.1016/j.ceramint.2021.12.247.

- [29] K. Zhang, J. Chen, W. Feng, C. Wang, Y.N. Zhou, Y. Xia, Constructing solid electrode-electrolyte interfaces in high-voltage Li|LiCoO₂ batteries under dualadditive electrolyte synergistic effect, J. Power Sources 553 (2023), 232311, https://doi.org/10.1016/j.jpowsour.2022.232311.
- [30] Z. Sun, H. Zhou, X. Luo, Y. Che, W. Li, M. Xu, Design of a novel electrolyte additive for high voltage LiCoO₂ cathode lithium-ion batteries: lithium 4-benzonitrile trimethyl borate, J. Power Sources 503 (2021), 230033, https://doi.org/10.1016/ i.joowsour.2021.230033.
- [31] J. Zhang, P.F. Wang, P. Bai, H. Wan, S. Liu, S. Hou, X. Pu, J. Xia, W. Zhang, Z. Wang, B. Nan, X. Zhang, J. Xu, C. Wang, Interfacial design for a 4.6V high-voltage single-crystalline LiCoO₂ cathode, Adv. Mater. 34 (2022) 1–12, https://doi.org/10.1002/adma.202108353.
- [32] X. Ren, X. Zhang, Z. Shadike, L. Zou, H. Jia, X. Cao, M.H. Engelhard, B. E. Matthews, C. Wang, B.W. Arey, X.Q. Yang, J. Liu, J.G. Zhang, W. Xu, Designing advanced in situ electrode/electrolyte interphases for wide temperature operation of 4.5V Li|LiCoO₂ batteries, Adv. Mater. 32 (2020) 1–8, https://doi.org/10.1002/adms.202004888
- [33] Y. Yan, S. Weng, A. Fu, H. Zhang, J. Chen, Q. Zheng, B. Zhang, S. Zhou, H. Yan, C. W. Wang, Y. Tang, H. Luo, B.W. Mao, J. Zheng, X. Wang, Y. Qiao, Y. Yang, S. G. Sun, Tailoring electrolyte dehydrogenation with trace additives: stabilizing the LiCoO₂ cathode beyond 4.6 v, ACS Energy Lett. 7 (2022) 2677–2684, https://doi.org/10.1021/acsenergylett.2c01433.
- [34] A. Fu, J. Lin, Z. Zhang, C. Xu, Y. Zou, C. Liu, P. Yan, D.Y. Wu, Y. Yang, J. Zheng, Synergistical stabilization of Li metal anodes and LiCoO₂ cathodes in high-voltage Li||LiCoO₂ batteries by potassium selenocyanate (KSeCN) additive, ACS Energy Lett. 7 (2022) 1364–1373, https://doi.org/10.1021/acsenergylett.2c00316.
- [35] J. Lee, Y.J. Kim, H.S. Jin, H. Noh, H. Kwack, H. Chu, F. Ye, H. Lee, H.T. Kim, Tuning two interfaces with fluoroethylene carbonate electrolytes for highperformance Li/LCO batteries, ACS Omega 4 (2019) 3220–3227, https://doi.org/ 10.1021/acsomega.8b03022.
- [36] J. Hu, Y. Ji, G. Zheng, W. Huang, Y. Lin, L. Yang, F. Pan, Influence of electrolyte structural evolution on battery applications: cationic aggregation from dilute to high concentration, Aggregate 3 (2022) 1–21, https://doi.org/10.1002/agt2.153.
- [37] J. Zhuang, X. Wang, M. Xu, Z. Chen, M. Liu, X. Cheng, W. Li, A self-healing interface on lithium metal with lithium difluoro (bisoxalato) phosphate for enhanced lithium electrochemistry, J. Mater. Chem. A 7 (2019) 26002–26010, https://doi.org/10.1039/c9ta09539j.
- [38] L. Li, H. Duan, L. Zhang, Y. Deng, G. Chen, Optimized functional additive enabled stable cathode and anode interfaces for high-voltage all-solid-state lithium batteries with significantly improved cycling performance, J. Mater. Chem. A 10 (2022) 20331–20342. https://doi.org/10.1039/d2ta03982f.
- [39] L. Li, J. Wang, L. Zhang, H. Duan, Y. Deng, G. Chen, Rational design of a heterogeneous double-layered composite solid electrolyte via synergistic strategies of asymmetric polymer matrices and functional additives to enable 4.5 V all-solidstate lithium batteries with superior performance, Energy Storage Mater. 45 (2022) 1062–1073, https://doi.org/10.1016/j.ensm.2021.10.047.
- [40] P. Shi, F. Liu, Y.Z. Feng, J. Zhou, X. Rui, Y. Yu, The synergetic effect of lithium bisoxalatodifluorophosphate and fluoroethylene carbonate on dendrite suppression for fast charging lithium metal batteries, Small 16 (2020) 1–8, https://doi.org/ 10.1002/smll.202001989.
- [41] J. Wang, D. Zhao, Y. Cong, N. Zhang, P. Wang, X. Fu, X. Cui, Analyzing the mechanism of functional groups in phosphate additives on the interface of LiNi_{0.8}Co_{0.15}Al_{0.05}O₂cathode materials, ACS Appl. Mater. Interfaces 13 (2021) 16939–16951, https://doi.org/10.1021/acsami.0c21535.
- [42] D. Zhao, J. Wang, P. Wang, H. Liu, S. Li, Regulating the composition distribution of layered SEI film on Li-ion battery anode by LiDFBOP, Electrochim. Acta 337 (2020), 135745, https://doi.org/10.1016/j.electacta.2020.135745.
- (2020), 135745, https://doi.org/10.1016/j.electacta.2020.135745.
 [43] T. Yang, H. Zeng, W. Wang, X. Zhao, W. Fan, C. Wang, X. Zuo, R. Zeng, J. Nan, Lithium bisoxalatodifluorophosphate (LiBODFP) as a multifunctional electrolyte additive for 5 v LiNi_{0.5}Mn_{1.5}O₄-based lithium-ion batteries with enhanced electrochemical performance, J. Mater. Chem. A 7 (2019) 8292–8301, https://doi.org/10.1039/c9ta01293a
- [44] Y. Li, B. Cheng, F. Jiao, K. Wu, The roles and working mechanism of salt-type additives on the performance of high-voltage lithium-ion batteries, ACS Appl. Mater. Interfaces 12 (2020) 16298–16307, https://doi.org/10.1021/ acsami.9b22360.
- [45] J. Xie, Y.C. Lu, A retrospective on lithium-ion batteries, Nat. Commun. 11 (2020) 9–12, https://doi.org/10.1038/s41467-020-16259-9.

- [46] J. Liu, B. Yuan, N. He, L. Dong, D. Chen, S. Zhong, Y. Ji, J. Han, C. Yang, Y. Liu, W. He, Reconstruction of LiF-rich interphases through an anti-freezing electrolyte for ultralow-temperature LiCoO₂ batteries, Energy Environ. Sci. (2022) 1024–1034, https://doi.org/10.1039/d2ee02411j.
- [47] R. Xu, X. Shen, X.X. Ma, C. Yan, X.Q. Zhang, X. Chen, J.F. Ding, J.Q. Huang, Identifying the critical anion–cation coordination to regulate the electric double layer for an efficient lithium-metal anode interface, Angew. Chem. Int. Ed. 60 (2021) 4215–4220, https://doi.org/10.1002/anie.202013271.
- [48] K. Chen, M. Lei, Z. Yao, Y. Zheng, J. Hu, C. Lai, C. Li, Construction of solid-liquid fluorine transport channel to enable highly reversible conversion cathodes, Sci. Adv. 7 (2021) 1–17, https://doi.org/10.1126/sciadv.abj1491.
- [49] S. Li, W. Zhang, Q. Wu, L. Fan, X. Wang, X. Wang, Z. Shen, Y. He, Y. Lu, Synergistic dual-additive electrolyte enables practical lithium-metal batteries, Angew. Chem. Int. Ed. 59 (2020) 14935–14941, https://doi.org/10.1002/anie.202004853.
- [50] T. Li, X.Q. Zhang, N. Yao, Y.X. Yao, L.P. Hou, X. Chen, M.Y. Zhou, J.Q. Huang, Q. Zhang, Stable anion-derived solid electrolyte interphase in lithium metal batteries, Angew. Chem. Int. Ed. 60 (2021) 22683–22687, https://doi.org/ 10.1002/anie.202107732.
- [51] M. Shibuya, M. Okamoto, S. Fujita, M. Abe, Y. Yamamoto, Boron-catalyzed double hydrofunctionalization reactions of unactivated alkynes, ACS Catal. 8 (2018) 4189–4193, https://doi.org/10.1021/acscatal.8b00955.
- [52] K. Bläsing, J. Bresien, R. Labbow, A. Schulz, A. Villinger, A dimer of hydrogen cyanide stabilized by a Lewis acid, Angew. Chem. Int. Ed. 57 (2018) 9170–9175, https://doi.org/10.1002/anie.201804193.
- [53] M. Nie, L. Madec, J. Xia, D.S. Hall, J.R. Dahn, Some Lewis acid-base adducts involving boron trifluoride as electrolyte additives for lithium ion cells, J. Power Sources 328 (2016) 433–442, https://doi.org/10.1016/j.jpowsour.2016.08.048.
- [54] Q. Li, W. Xue, X. Sun, X. Yu, H. Li, L. Chen, Gaseous electrolyte additive BF3 for high-power Li/CFx primary batteries, Energy Storage Mater. 38 (2021) 482–488, https://doi.org/10.1016/j.ensm.2021.03.024.
- [55] W.P. Wang, J. Zhang, Y.X. Yin, H. Duan, J. Chou, S.Y. Li, M. Yan, S. Xin, Y.G. Guo, A rational reconfiguration of electrolyte for high-energy and long-life lithium-chalcogen batteries, Adv. Mater. 32 (2020) 1–11, https://doi.org/ 10.1002/adma.202000302.
- [56] C. Wang, H. Zhang, S. Dong, Z. Hu, R. Hu, Z. Guo, T. Wang, G. Cui, L. Chen, High polymerization conversion and stable high-voltage chemistry underpinning an in situ formed solid electrolyte, Chem. Mater. 32 (2020) 9167–9175, https://doi.org/ 10.1021/acs.chemmater.0c02481.
- [57] Z. Bi, L. Huo, Q. Kong, F. Li, J. Chen, A. Ahmad, X. Wei, L. Xie, C.M. Chen, Structural evolution of phosphorus species on graphene with a stabilized electrochemical interface, ACS Appl. Mater. Interfaces 11 (2019) 11421–11430, https://doi.org/10.1021/acsami.8b21903.
- [58] W. Liu, H. Gao, Z. Zhang, Y. Zheng, Y. Wu, X. Fu, J. Su, Y. Gao, CoP/Cu3P heterostructured nanoplates for high-rate supercapacitor electrodes, Chem. Eng. J. 437 (2022), 135352, https://doi.org/10.1016/j.cei.2022.135352.
- 437 (2022), 135352, https://doi.org/10.1016/j.cej.2022.135352.
 [59] X. Liu, L. Zhao, H. Xu, Q. Huang, Y. Wang, C. Hou, Y. Hou, J. Wang, F. Dang, J. Zhang, Tunable cationic vacancies of cobalt oxides for efficient electrocatalysis in Li–O₂ batteries, Adv. Energy Mater. 10 (2020) 1–10, https://doi.org/10.1002/aenm_202001415.
- [60] W. Kong, J. Zhang, D. Wong, W. Yang, J. Yang, C. Schulz, X. Liu, Tailoring Co3d and O2p band centers to inhibit oxygen escape for stable 4.6V LiCoO₂ cathodes, Angew. Chem. Int. Ed. 60 (2021) 27102–27112, https://doi.org/10.1002/anje.202112508
- [61] A. Pöppl, G. Völkel, ESR and Photo-ESR investigations of zinc vacancies and interstitial oxygen ions in undoped ZnO ceramics, Phys. Status Solidi 125 (1991) 571–581, https://doi.org/10.1002/pssa.2211250218.
- [62] B. Jin, Z. Cui, A. Manthiram, *In situ* interweaved binder framework mitigating the structural and interphasial degradations of high-nickel cathodes in lithium-ion batteries, Angew. Chem. Int. Ed. (2023) 78712, https://doi.org/10.1002/ anie 202301241
- [63] G.G. Amatucci, J.M. Tarascon, L.C. Klein, CoO₂, the end member of the Li x CoO₂ solid solution, J. Electrochem. Soc. 143 (1996) 1114–1123, https://doi.org/10.1149/1.1836594.
- [64] Q. Zhao, S. Stalin, L.A. Archer, Stabilizing metal battery anodes through the design of solid electrolyte interphases, Joule 5 (2021) 1119–1142, https://doi.org/ 10.1016/j.joule.2021.03.024.
- [65] H. Zhang, Z. Song, J. Fang, K. Li, M. Zhang, Z. Li, L. Yang, F. Pan, Electrolyte optimization for graphite anodes toward fast charging, J. Phys. Chem. C 127 (2023) 2755–2765, https://doi.org/10.1021/acs.jpcc.2c08357.